

Lawrence Berkeley National Laboratory

LBL Publications

Title

Gravity current analyzer for lock-release experiments

Permalink

<https://escholarship.org/uc/item/7mx8p1q3>

Journal

Journal of Applied Water Engineering and Research, ahead-of-print(ahead-of-print)

ISSN

2324-9676

Authors

de Carvalho Bueno, Rafael
da Silva, Nathan Streisky
dos Santos, André Diniz
[et al.](#)

Publication Date

2024

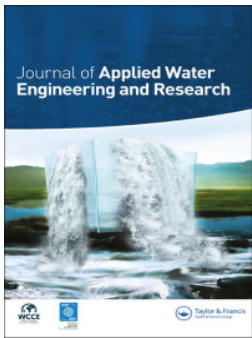
DOI

10.1080/23249676.2024.2340972

Copyright Information

This work is made available under the terms of a Creative Commons Attribution-NonCommercial License, available at <https://creativecommons.org/licenses/by-nc/4.0/>

Peer reviewed





Gravity current analyzer for lock-release experiments

Rafael de Carvalho Bueno, Nathan Streisky da Silva, André Diniz dos Santos & Tobias Bernward Bleninger


To cite this article: Rafael de Carvalho Bueno, Nathan Streisky da Silva, André Diniz dos Santos & Tobias Bernward Bleninger (25 Apr 2024): Gravity current analyzer for lock-release experiments, Journal of Applied Water Engineering and Research, DOI: [10.1080/23249676.2024.2340972](https://doi.org/10.1080/23249676.2024.2340972)

To link to this article: <https://doi.org/10.1080/23249676.2024.2340972>

 View supplementary material [↗](#)

 Published online: 25 Apr 2024.


 Submit your article to this journal [↗](#)

 View related articles [↗](#)

 View Crossmark data [↗](#)



Gravity current analyzer for lock-release experiments

Rafael de Carvalho Bueno ^a, Nathan Streisky da Silva^a, André Diniz dos Santos^a and Tobias Bernward Bleninger^{a,b}

^aGraduate Program in Environmental Engineering, Federal University of Paraná, Curitiba, Brazil; ^bDepartment of Environmental Engineering, Federal University of Paraná, Curitiba, Brazil

ABSTRACT

Analyzing gravity currents and stratified flows thoroughly is a time-consuming task, particularly in engineering and educational contexts. Despite the availability of numerous tools for studying stratified flows, there is currently no software dedicated to analyzing gravity currents, integrating flow characterization with theoretical and empirical analyses. This study introduces an open-source tool (Dyemonic), specifically designed for conducting in-depth analyses of gravity currents using a single recorded video. The software incorporates a particle image velocimetry routine to examine the velocity field of the gravity current and the sediment particle transport, offering essential physical indices and categorization based on existing literature. Data from modeling results and laboratory experiments are used to perform calibration, validation, and sensitivity analyses. The findings demonstrate strong alignment with the existing gravity current literature, highlighting the effectiveness of the software in characterizing gravity currents. Dyemonic emerges as a robust, user-friendly, and versatile tool suitable for educational and research endeavors.

ARTICLE HISTORY

Received 27 October 2023
Accepted 5 April 2024

KEYWORDS

Gravity current; laboratory flumes; sediment resuspension; PIV; density current



1. Introduction


In lakes and reservoirs, the gravity current plays a crucial role in aquatic ecosystems and biogeochemical cycling by redistributing phytoplankton and zooplankton organisms (Scotti and Pineda 2007) and causing sediment resuspension and chemical contaminant dispersion (Eames et al. 2001; Kyrousi et al. 2018). The turbulence level increases due to the evolution of the gravity current, which can also influence mean flow and increase mixing in the benthic boundary layer due to the change in the structure of the turbulence (Buckee et al. 2001). In the ocean, these currents are often generated by salinity differences, which promote the propagation of less salty water on the ocean surface, influencing large-scale ocean circulation and consequently playing an important role in the physical climate system (Legg et al. 2009; Jkedorasik and Kowalewski 2019). Large turbidity currents have been observed on the upper continental slope due to sediment slumps, which affect sediment transport on the ocean shore (Pickering et al. 1992; Wynn et al. 2000; Azpiroz-Zabala et al. 2017). Gravity currents are also observed in the atmosphere, such as squalls (Auer and Sand 1966), sea-breeze fronts (van der Wiel et al. 2017), and avalanches

(Hutter 1996), which play a pivotal role in the transport of atmospheric pollutants and local turbulence (Arrilaga et al. 2018; Mitxelena 2020).

Gravity current is a fundamental fluid mechanics phenomenon, often used to exemplify buoyancy-driven flow, and it is included in most textbooks that introduce the basis of stratified flows. Gravity currents can be easily reproduced in laboratory tanks. The flow has a distinct lobate head formed by a series of lobes and clefts that generate frontal vortices and shear instabilities (Hallworth et al. 1993). The head is followed by a shallower layer with low mixing with the ambient fluid, where intense mixing occurs at the back of the gravity current head (Simpson and Britter 1979; Best et al. 2001). The propagation of the gravity current increases turbulence, playing a crucial role in the geomorphological changes of the sediment layer (Parker et al. 1987) (Figure 1).

Although gravity currents have a distinct shape, their form and inner velocity field can be strongly modified depending on environmental conditions, bathymetry, Reynolds number, and stratification profile, among others (Simpson 1982). Gravity currents have been widely studied numerically (Härtel et al. 2000; Cantero

CONTACT Rafael de Carvalho Bueno  rafael.bueno@ufpr.br  Laboratory of Sensor Technology and Limnological Research. Rua Química – Centro Politécnico – CEHPAR UFPR, Jardim das Américas, Curitiba, Brazil

 Supplemental data for this article can be accessed online at <https://doi.org/10.1080/23249676.2024.2340972>.

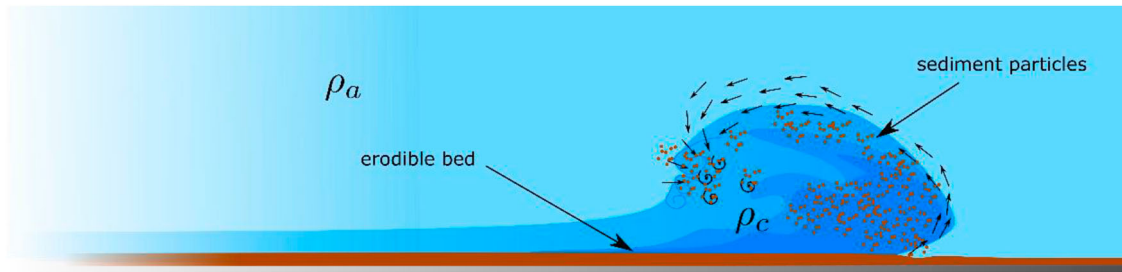


Figure 1. Sketch of a typical bottom gravity current ($\rho_c > \rho_a$) advancing in an erodible bed. ρ_a and ρ_c are the ambient water density (light blue) and the current water density (dark blue), respectively. Arrows along the head illustrate the velocity vectors of the ambient fluid influenced by the evolution of the current.

et al. 2007; Ooi et al. 2007; Paik et al. 2009; Gerber et al. 2011) and experimentally (Benjamin 1968; Rottman and Simpson 1983; Shin et al. 2004) in the last 80 years. Despite the fact that gravity currents are often observed in natural environments, many studies have been conducted in laboratory tanks to highlight the main aspects that could not be revealed in field observations. Many fundamental aspects of gravity currents have been revealed, especially for simple conditions (Benjamin 1968; Hacker et al. 1996; Shin et al. 2004). Despite the huge literature, the quantitative analysis of gravity currents in laboratory tanks requires a costly and time-consuming effort to process and analyze results from laboratory experiments. There is a lack of adequate tools to investigate the propagation of gravity currents generated in laboratory tanks, combining a consistent and universal technique with theoretical results from the wide literature.

The aim of this paper is to present and describe an open-source tool with a simple and intuitive graphical user interface for analyzing gravity currents in laboratory flumes. Dynamic provides a detailed characterization of gravity currents by deriving important physical indices and providing a detailed analysis of the inner velocity field of the currents using particle image velocimetry (PIV) and a front-tracker algorithm. The software uses consistent techniques to allow analysis of dye-colored gravity currents under different conditions through a single video recorded laterally through a transparent wall. Software can also be used to analyze sediment particle transport with resuspension induced by gravity current.

The paper is organized as follows. Section 2 presents the relevant theoretical background of the gravity currents that are coupled with the software. The structure of the program, the input data, the data processing, and the output results are discussed in Section 3. The application and physical interpretation of the results provided by the software are described for two experiments in Section 4. The first experiment explores the

analysis of a gravity current traveling over a smooth bed, a classical gravity current experiment run with a video file generated from numerical simulation data. This case study is used to reveal the capabilities of Dynamic to describe the evolution of the gravity current. The second experiment consists of a series of laboratory experiments carried out in a rectangular tank with an erodible bed. These laboratory experiments are used to evaluate the influence of user-defined calibration parameters on the results generated by the software.

2. The dynamics of a gravity current

The gravity current, an ubiquitous three-dimensional buoyancy-driven flow, is characterized by a thinner body and a lobate head generated by a horizontal density variation, often associated with temperature and salinity stratification, which produces an unbalanced pressure difference, resulting in a driven horizontal motion.

One of the simplest experiments for gravity currents and one of the most studied is the constant volume lock exchange (Shin et al. 2004; Kyrousi et al. 2018), which is characterized by the fixed fluid volume ρ_c released into a stationary ambient fluid ρ_a (Figure 2(a)). Initially, the system is divided by a vertical barrier, in which a denser fluid is placed on one side, whilst the other is filled with a lighter fluid. The initial height h_o occupied by the denser fluid may vary depending on the experiment. When the barrier is removed, the denser fluid flows along the bottom of the channel, while the lighter fluid flows in the opposite direction along the surface. Depending on density and boundary conditions, the head of the gravity current may vary in shape and size, playing a crucial role in the dynamics of the gravity current.

One of the most important parameters for characterizing the dynamics of gravity currents assuming the Boussinesq condition is the bulk Froude number Fr , which characterizes the ratio between inertial and

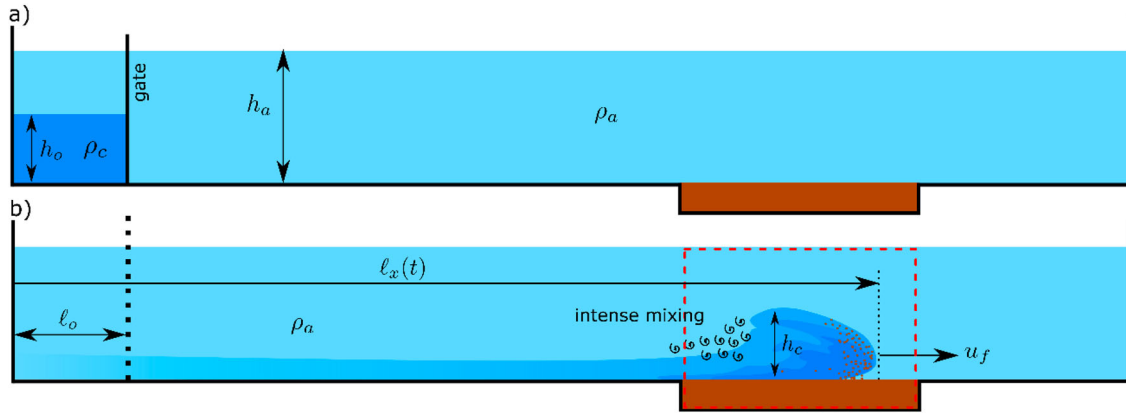


Figure 2. Sketch of a constant volume lock release in a deep ambient gravity current traveling in a rectangular flume above an erodible bed. The figure illustrates (a) the initial condition of the experiment with a gate positioned ℓ_o from the left end wall of the tank and (b) the evolution of the gravity current at ℓ_x , with head height h_c , propagating with speed u_f above the erodible bed. The tank is initially filled with fresh water (ρ_a) to a height of h_a . The current fluid (ρ_c) initially occupies $h_o \times \ell_o$ per width of the channel. Shear stress due to the evolution of the gravity current on the erodible bed promotes erosion (E) and deposition (D) of sediment particles.

gravitational forces:

$$Fr = \frac{u}{g'h'} \quad (1)$$

in which u is the reference current speed, h is the reference current height, and $g' = g\Delta\rho/\rho_c$ is the reduced gravity, where $g = 9.81 \text{ m s}^{-2}$ is the acceleration of gravity, and $\Delta\rho = \rho_c - \rho_a$ is the density difference between ambient fluids and current. The definition of the reference quantities may vary depending on the theoretical framework adopted, which should be defined depending on the gravity current conditions (e.g. currents released from a submerged shallow tank).

Despite the various ways to define Equation 1, in most cases, the current evolution may be divided into different phases according to the analysis of the Froude number. When the barrier is suddenly removed, the buoyancy forces set the heavier fluid in motion, accelerating the current horizontally. This accelerating phase occurs on a rapid time scale. After the acceleration phase, if the viscous forces are not important, the gravity current reaches the inertial slumping regime, in which the current travels at a constant speed. As the gravity current propagates longitudinally, increasing its extension, the current height h_c decreases proportionally, leading to a constant speed. Studies have shown that in this regime, the local Froude number depends on the relationship between the local height of the current and the depth of the ambient fluid, $\phi = h_c/h_a$:

$$Fr_f = \frac{u_f}{g'h_c} = \sqrt{\frac{\phi(2-\phi)(1-\phi)}{1+\phi}}, \quad (2)$$

in which u_f is the current front speed. At the limit of $\phi = 0.5$, the solution leads to $Fr = 0.5$. The local

height is unlikely to generate $\phi > 0.5$ without any external input energy. Furthermore, studies have shown that $\phi = 0.5$ is unlikely given the interfacial mixing of gravity currents that reduces the current height, limiting ϕ to 0.347 (Benjamin 1968).

This phase persists between 3 and 10 lock-lengths ℓ_o . Investigations have shown that this phase is strongly influenced by an internal bore generated due to wall reflection that propagates away from the volume of the lock, towards the current head (Rottman and Simpson 1983). New models have been proposed to account for the influence of the backward propagating wave. Studies have suggested that energy dissipation can be neglected for intermediate Reynolds numbers (Shin et al. 2004). In addition, observations have suggested that Fr_f is only dependent on the initial condition of lock release:

$$Fr_f = 0.5 \sqrt{\frac{h_o}{h_a} \left(2 - \frac{h_o}{h_a} \right)}. \quad (3)$$

In the limit of $h_o/h_a = 1$, Equation 3 yields the same value as obtained with the Benjamin model (Equation 2). For infinity deep ambient fluids ($\phi \approx 0$), the theoretical results differ approximately 40%.

This phase persists until the reflected propagating wave catches up with the gravity current front (Rottman and Simpson 1983). When the finite initial volume becomes important for the current front, the gravity current decelerates, reaching the self-similar stage. Although the denser fluid mixes with its surroundings, the initial buoyancy ($B_o = g'_o \ell_o h$) is conserved due to the increase in volume when the current flows away from the release.

The evolution of the current length ℓ_x has been estimated through dimension analysis for a plane ($n = 0$) and axisymmetric ($n = 1$) flow (Huppert and Simpson 1980; Rottman and Simpson 1983), which found that

$$\ell_x(t) = \xi(Fr_f)(g'_a h_o \ell_o)^{\frac{2-n}{6}} t^{2/(3+n)}, \quad (4)$$

in which $g'_a = g\Delta\rho/\rho_a$ is the reduced gravity parameterized by the ambient fluid and ξ is a dimensionless function, which has been estimated by many authors (Benjamin 1968; Grundy and Rottman 1985; Shin et al. 2004).

The Equation 4 indicates that the gravity current decelerates proportionally to $t^{-1/3}$ and $t^{-1/2}$ for the planar and axisymmetric currents, respectively. In this phase, the gravity current head decreases until the flow becomes laminar, leading to small mixing and no formation of billowing structures. Studies have demonstrated that Equation 4 presents good agreement for deep ambient gravity currents, which are obtained from partial depth release or long-time limits (Grundy and Rottman 1985).

As the gravity current decelerates, the Reynolds number decreases, and viscous forces start to play an important role in the evolution of the gravity current, further decreasing the height of the current. This phase is known as the *viscous phase*. As the Reynolds number decreases, the current is no longer controlled or even influenced by the current nose (Huppert 2006). The buoyancy force is completely balanced by viscous forces, causing a deceleration proportional to $t^{-4/5}$ (Huppert 1982). The time-scale for viscous phase is no longer described by the initial condition of the flow and is determined especially by properties related to viscous phase.

3. Methods

3.1. Input data processing

3.1.1. Water density and sediment particles identification

The water density is estimated based on grayscale values of frames from the input video and calibrated beforehand by the user. Dyanamic offers a calibration tool that generates a grayscale matrix from the initial condition, helping to define the grayscale range for density concentration (e.g. temperature and salinity). A detailed explanation of this procedure is provided in the user manual (de Carvalho Bueno et al. 2021). The fluid density is based on a direct linear regression that creates a relationship between the initial conditions. This approach assumes that the mixing event generates a density dilution that varies linearly with grayscale

values:

$$\rho(x, z) = \frac{\Delta\rho}{\Delta GS} GS(x, z) + \rho_c, \quad (5)$$

where $\Delta\rho = \rho_c - \rho_a$ is the density difference between current and ambient fluids, ΔGS is an grayscale user-defined calibration parameter, and GS is the local grayscale value. The software also provides the option for the user to define his own equation, which must be specified in a potential form. In this case, the user must find beforehand, based on the experimental calibration procedure, all three coefficients of the potential equation. This calibration procedure is explained in detail in the user manual.

When the erodible bed is analyzed, the user must calibrate and define a new grayscale range. Unlike the water density, every pixel that falls into the grayscale range of sediment is assumed to be an area occupied by sediment particles. Therefore, the grayscale of sediment particles cannot overlap the grayscale range of fluid volume, so the material and color of the sediment particle should be chosen carefully.

Dyanamic also applies a filtering procedure for each frame to minimize the influence of shadow regions and scratches on the tank wall. The filter scheme subtracts initial conditions and consecutive frames to identify when the grayscale that falls into the gravity current concentration range indicates a false concentration due to the variation of the background intensity. All false concentrations due to background noise are assumed to be part of the ambient fluid (ρ_a).

3.1.2. Current front

Dyanamic is coupled with a concentration interface tracker that defines the front evolution of the gravity current for different heights specified by the user. The software tracks from right to left the evolution of the current front by following the background fluid, assuming a variation up to 1% of the initial background density fluid. A consistency procedure is applied to guarantee that the current always travels in positive x-direction, excluding the influence of the small density difference generated in the body of the gravity current. The front speed of the current is obtained as a means of consecutive measurements. The software also provides the theoretical gravity current speed for the three distinct stages (slumping, self-similar, and viscous phases).

To calculate the local Froude number (Equations 1–3), the height of the current is measured based on the equivalent depth profiles for each time step. Dyanamic identifies the interface similarly to the computation of the front velocity position. The software identifies the interface of gravity currents when the salinity

concentration of the cell value falls below 0.005% of the initial condition of the ambient fluid density for each horizontal grid, in which the height of the head is defined as the calculated maximum height. The difference threshold has been set differently from the current front position because mixing events play an important role in the current body, which can lead to incorrect estimation of the current height. Furthermore, the software also provides results assuming that the head height is given by half of the initial current height ($h_0/2$).

The program also computes the short-time Fourier transform normalized by the spectrum resolution to analyze the harmonic components of the front position (in x-direction). The signal is divided into overlapped segments (50%) using the Hamming function and averaged. The size of the window must be specified by the user. The default value (0 s) indicates that the signal is not partitioned.

The significance of spectral peaks is estimated through the mean red noise spectrum from the front evolution of the gravity current by assuming a chi-square test (Bernhardt and Kirillin 2013). From the one-lag autoregressive coefficient, the program estimates the power spectral density of a red noise function. To estimate confidence levels, Dynamic performs the chi-square test with a confidence level of 95%. For more details on the numerical procedure, see the user manual (de Carvalho Bueno et al. 2021).

3.1.3. Particle image velocimetry

Dynamic is coupled with a particle image velocimetry code (PIV) (Liberzon et al. 2020), which is a state-of-the-art non-intrusive technique for flow visualization that performs a complete analysis of the inner velocity field of gravity currents. When users wish to use PIV measurements, the fluid must be seeded with small tracer particles, usually of the order of 10–100 microns. For high-accuracy measurement, the experimental setup should contain a pulse laser to ensure a high-quality illumination of the fluid with entrained particles, and the video must be recorded with a CMOS camera (Raffel et al. 2018; Ben-Gida et al. 2020). However, for general analysis, even simple setups can be sufficiently used to describe the evolution of gravity currents.

The software uses a zero-order displacement predictor cross-correlation algorithm from the OpenPIV source code (Ben-Gida et al. 2020; Liberzon et al. 2020), which has been tested for several applications (Hadad and Gurka 2013; Yarom and Sharon 2014; Verso et al. 2017)

To improve the quality of PIV measurements, Dynamic also applies an adaptive mean thresholding filter to neglect the influence of grayscale changes due to variation in salinity concentration, highlighting only small tracer particles. The software uses a peak-to-peak signal-to-noise ratio, estimating the ratio between peaks to identify the best correlation based on shifting parameters.

The algorithm identifies particles using an overlapped fixed interrogation window, in which the user must specify the size of the interrogation window and the percentage of overlap as a calibration parameter. The default values are 8 and 16 pixels for the window and the overlap size, respectively. The scaling factor is defined based on the resolution of the camera (pixel size) and the user-defined size of the analyzed area. The whole PIV computation is performed at a user-defined time step and is limited by the temporal resolution of the video camera.

To eliminate spurious velocity vectors, the software identifies the outliers of velocity vectors by comparing the ratio between the two highest peaks on the correlation map, a *signal-to-noise* ratio filtering procedure from OpenPIV open source library (Liberzon et al. 2020). Sensitivity is defined by the user-defined noise ratio threshold parameter, which is used to identify outlier velocity vectors. The default value for the noise ratio threshold is 1.3, but the user should try to find the best value.

Outliers are replaced by weighted averages of valid neighbor vector values. This method uses an interactive in-painting algorithm in which the user defines the number of repetitions. The default value is 10. The weight of the average procedure is based on the size of the kernel function, which must also be specified by the user. The default value is 2. For more details on the technique used by Dynamic to obtain PIV measurements, see the user manual, available at <https://sites.google.com/view/dynamic/manual>, and the OpenPIV library (Ben-Gida et al. 2020; Liberzon et al. 2020). An example of PIV measurements obtained from Dynamic is demonstrated for a particular case study in section 4.1.2.

3.1.4. Sediment transport

Sediment particles are identified similarly to the density current, based on user-defined calibration parameters. The software basically computes the mobility of sediment particles for specific vertical grids, describing the longitudinal and vertical transport. When the value is above the reference level, it indicates a potential erosion mechanism of the erodible bed layer. Values above the reference level indicate a bedload transport or a

Table 1. Output parameters provided by Dyynamic.

Output variables	Reference
Water density field	Equation 5
Velocity field	Equation S8
Front current evolution	Equation S2
Power spectral density of current position	Equation S6
Front current speed	Equation S1
Maximum current height	Equation S3
Bulk and Local Froude number	Equation 1
Richardson number	Equation S4
Theoretical Froude number for slumping stage	Equations 2 and 3
Theoretical front position for self-similar stage	Equation 4
Overturns density displacement	Equation S5
Total sediment area above bed at position x	Equation S7

resuspension process. A detailed analysis of the results provides a good estimate of the transport of sediment particles. An example of this analysis is presented in detail for a case study in Section 4.1.3.

3.1.5. Output data

The software provides the time-series of many variables, including density field, gravity current evolution, Froude number, Richardson number, current head height, Thorpe scale, and velocity field, as well as time-scale of phases. In addition, when enabled, the Dyynamic also provides information about the transport of sediment particles above the bed. The most important

calculations provided by Dyynamic are summarized in Table 1.

3.2. Input data and configuration

Dyynamic requires a video file input (.mp4), which describes the propagation of the gravity current from the front face of the channel. The video must contain the entire height of the ambient fluid, from top to bottom (Figure 3). Detailed instructions on how to record the video are provided in the user manual. The user must specify the temporal resolution at which the video will be analyzed, the maximum resolution being defined by frame per second (FPS) of the recorded video.

Additional user-defined parameters must be specified in the graphical user interface (GUI). These include ambient density ρ_a , gravity current density ρ_c , horizontal and vertical video length, initial current height (h_o), lock length (l_o), virtual length (distance between the end of the lock length and the area analyzed) and fluid kinematic viscosity ν . The user must also specify the user-adjustable calibration parameters: maximum and minimum grayscale values associated with the fluid initial condition, and two additional parameters must be specified in the case of experiments with an erodible

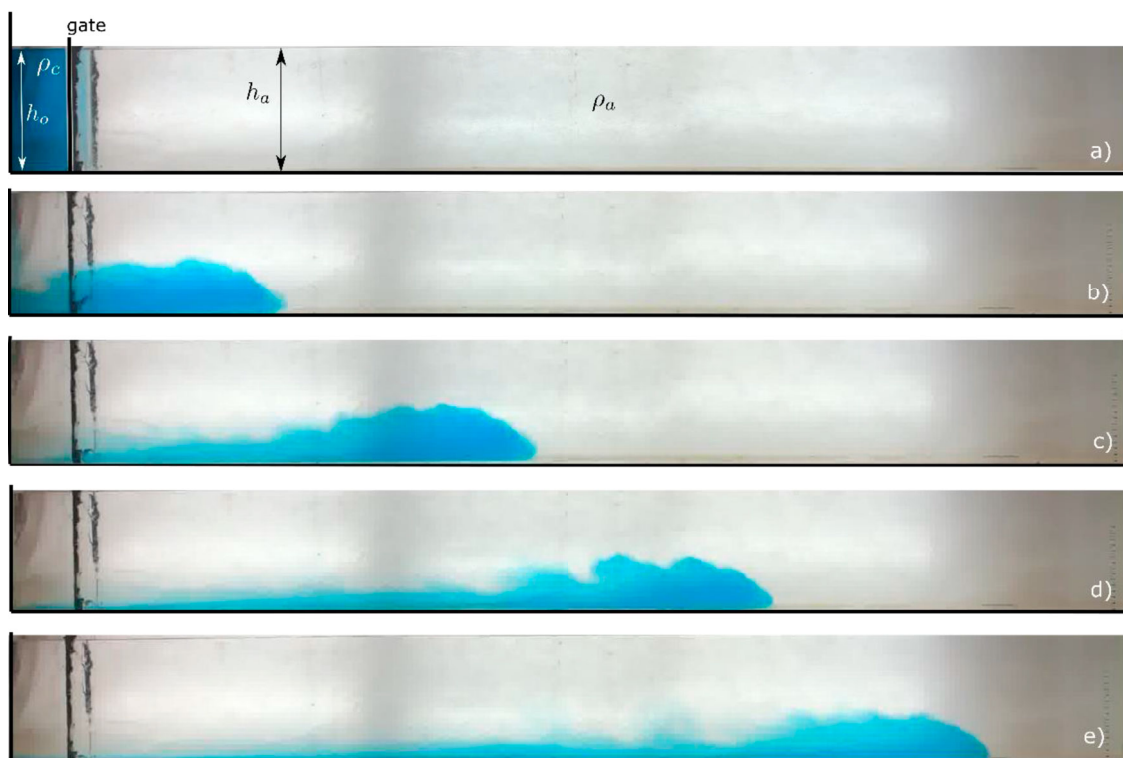


Figure 3. Sequence of images from the video applied to the software, showing the evolution of the gravity current in the experiment from (a) the initial experimental setup. The following snapshots represent (b) $t = 5$ s, (c) 10 s, (d) 15 s, and (e) 20 s from the vertical lock release.

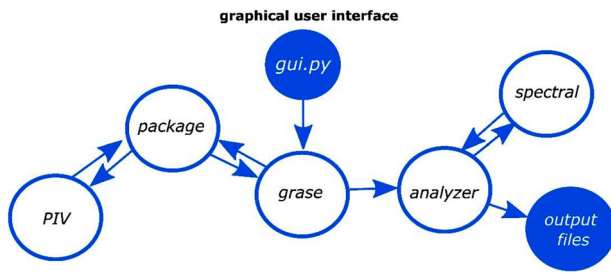


Figure 4. Dynamic subprograms.

bed, covering the grayscale associated with sediment particles.

The user has the option to define a linear model or a potential model to describe density variation based on grayscale values. For the potential model, the user must also specify three coefficients of the potential equation. For PIV measurement, users must specify several calibration parameters: window size (default is 16), overlap percentage (default is 8), noise ratio threshold (default is 1.3), number of iterations (default value is 10), kernel size (default value is 2), maximum value for outliers (default value is 255), block size (default value is 5) and weighted average constant (default value is 5). For more details on each user-adjustable calibration parameter for PIV measurements, see the user manual.

In order to analyze the front evolution of the current, the user must specify a maximum of three heights in which the current front will be analyzed in detail. In addition, in order to reduce the number of output files, the user can also choose which output file will be generated frame-by-frame (e.g. field density, overturn density displacement, sediment variation, sediment transport, and PIV measurements). For all these quantities, the user has the option to generate text files (.txt) or/and graphical images (.png). Time-series output results are generated in both formats and do not need to be specified by the user. Finally, the settings defined in the GUI can be saved to a file (.gcs), which can be imported to run the same experiment again.

3.3. Program structure

Dynamic is an open-source software implemented in Python that is used to investigate the dynamic of the gravity current generated in laboratory tanks and by numerical simulations based on a single recorded video. The software is structured into six modules (Figure 4), including a graphical user interface (GUI).

The *grase* module (*grase.py*) is responsible for data exchange between computational modules, including communication with the GUI code (*grase_gui.py*). The *package* module (*grase_package.py*) processes the

video and extracts frames. When PIV measurements are enabled, frames from *grase_package.py* are sent to the PIV algorithm (*grase_piv.py*) to compute the PIV measurements. The preprocessed data are sent back to the *grase* module, which then follows to the *analyzer* (*grase_analyzer.py*), responsible for computing most output results. The *analyzer* module is responsible for separating the gravity current from the sediment particles and computing most physical quantities, including the front velocity, current height, the Froude number, Thorpe scales and Reynolds number. Finally, spectral analysis is performed on *grase_spectral.py*, which sends the results to the *analyzer* module.

All Dynamic source codes can be found in the GitHub repository, located at <https://github.com/buenorc/dynamic.git>, which is distributed under the MIT license. The user manual and study cases can be downloaded from Dynamic's website (<https://sites.google.com/view/dynamic/dynamic>).

4. Results and discussions

4.1. Case studies

4.1.1. Dynamic validation

The capabilities of Dynamic to describe the evolution of gravity currents is investigated through a bidimensional non-hydrostatic numerical simulation of a fixed fluid volume gravity current. The simulation of a gravity current was carried out in a rectangular tank (e.g. Figures 2 and 3(a)), 2 m long and 20 cm deep. The stratification of the density was specified by a salinity change, corresponding to an initial and ambient current density of 1006.8 kg m^{-3} and 1034.5 kg m^{-3} , respectively. The lock length ℓ_o was placed 13 cm from the right wall, and the simulation was carried out as a full depth release experiment ($h_o = 20 \text{ cm}$).

The gravity current was simulated by the nonhydrostatic solver of Delft3D-FLOW (Deltares 2014) with a time step of 0.006 s. Previous studies have shown that Delft3D is skilled at simulating baroclinic flow propagation and salinity and temperature transport due to density driven flows in rectangular tanks (Gerritsen et al. 2007).

The simulation was established in horizontal and vertical Cartesian grid cells of size 1.25 and 1.75 cm, respectively. Eddy diffusivity and Eddy viscosity were calculated using the $\kappa - \varepsilon$ turbulence closure model, without background values for viscosity and diffusivity, as used in a previous validation study (Gerritsen et al. 2007).

A video file containing the evolution of the gravity current was generated from the Delft3D results density

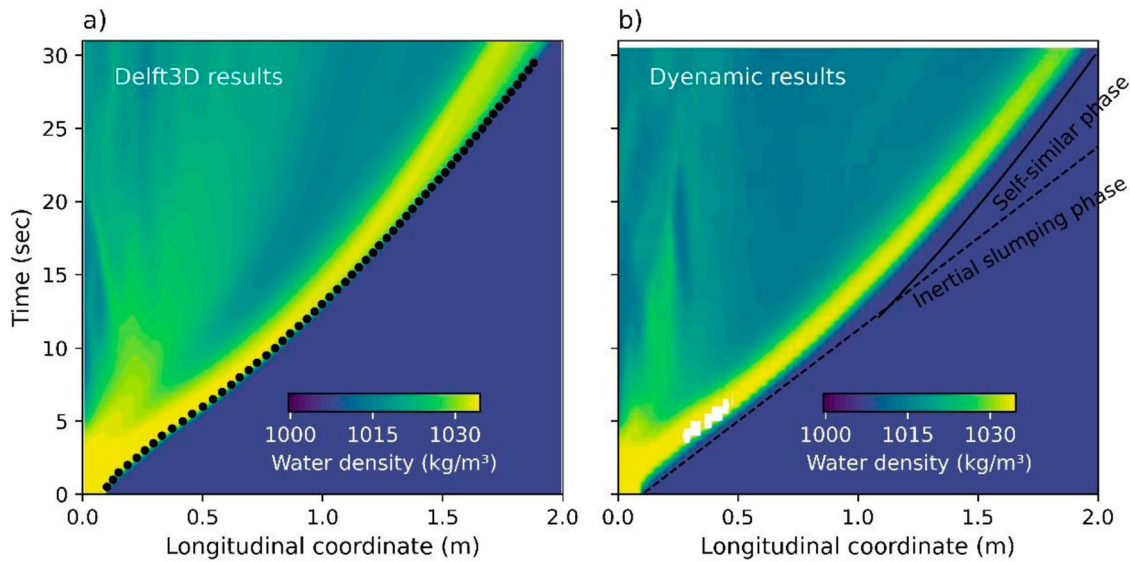


Figure 5. Evolution of the water density as a function of longitudinal position and time captured 1 cm above the bottom. The contour plots show the water density of (a) Delft3D and (b) Dyynamic results. Black dots show the evolution of the current front measured by Dydynamic. Inertial slumping phase (Equation 3) and self-similar phase (Equation 4) are illustrated by dashed and solid lines, respectively.

output file through Delft3D-QUICKPLOT, using a smoothed *L&B blue* color map with a resolution of 985×88 pixels. Dydynamic was run with a temporal resolution of 0.5 s using the linear density model. Additional information to run this case study in the Dydynamic is available in the Supplementary Material.

As soon as the barrier is released, the inherent baroclinic pressure gradient induces a bottom gravity current. Potential energy is rapidly converted to kinetic energy, accelerating the current front towards the other side of the tank. The acceleration phase lasts for 1.5 s and is followed by the inertial slumping regime, in which the current propagates steadily, at a constant speed of approximately 8 cm s^{-1} (Figure 4(a)). After this stage, the current reaches the self-similar regime, when the current decelerates due to the entrainment and mixing mechanisms, which reduces the density of the current, and consequently, the current speed. The propagation of the gravity current is illustrated through the evolution of the current density as a function of position and time 1 cm above the bottom (Figure 5).

The front position of the gravity current head is well captured by Dydynamic (Figure 5(a)), which also provides, from Equations 2 to 4, the theoretical moment of transition from a slumping to a self-similar stage, at $\ell_x = 90 \text{ cm}$ (Hallworth et al. 1996), which is consistent with measurements performed by the software. The mean error associated with the front speed (difference between the value calculated from Delft3D and the one estimated by Dydynamic) may vary between 3% to 19%, for Dydynamic time step varying from 0.3 sec to

0.7 sec (Figure 6(a)). This error variation is associated to discretization of time step, for more clarification see Sectio 4.1.3 (Calibration of temporal resolution).

The Dydynamic described, based on the linear density model, the evolution of the current density, which is in good agreement with the results of Delft3D (Figure 6(b)). The mean error of the density field at 1 cm above the bottom is around 14%, which is equivalent to 3.9 kg m^{-3} . A smaller error has been observed in the current head ($1.4\% \pm 0.3\%$). Most errors in Dydynamic ($48\% \pm 11\%$) are observed in the vicinity of the current front due to the user-defined temporal resolution. Since the interface has a strong density gradient, the time delay due to the temporal resolution of Dydynamic may generate high errors in the interface between two consecutive frames. The current body has a mean error of 23%. The error observed along the current body is associated with the grayscale calibration procedure, which may limit the tracking of areas of low concentration (Figure 6(b)). This occurs because of the low-contrast colors between current and ambient fluids. Dydynamic evaluates the contrast-color through the ratio between ambient and gravity current grayscales. This case study has a contrast-color ratio equal to 6.41. The lower this ratio, the lower the contrast between ambient and gravity current fluids, which may reduce the performance of the software.

The conservation of mass is analyzed for different frames by integrating the water density along the tank area. For this case study, the mass decreases by 0.1 kg m^{-1} during the first 30 s (Figure 7). This limitation

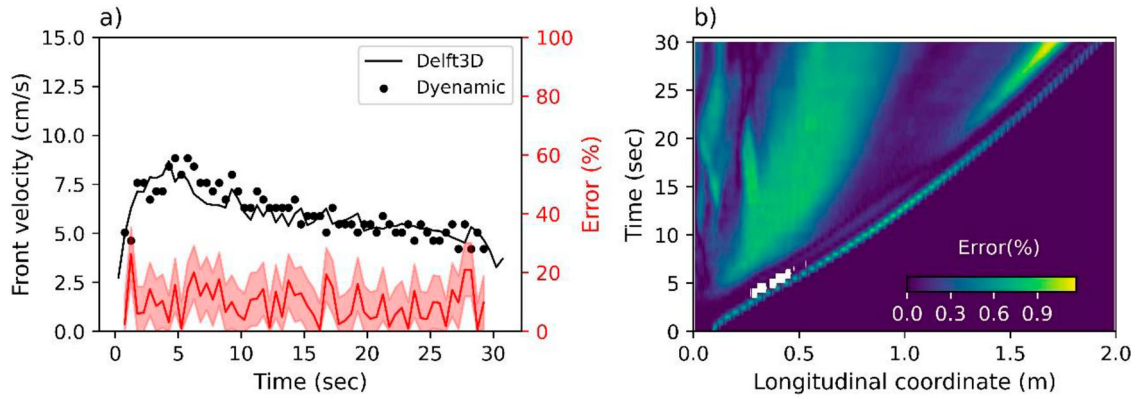


Figure 6. Validation of the speed of the gravity current and the density of the water. (a) Validation of the front velocity. The black dots represent the front speed captured by Dyenamic at 1 cm from the bottom. The black solid line shows the current computed numerically by Delft3D, in which the front speed was defined as the mean velocity of a window of 6 numerical grid cells detected within the maximum density difference region. The red line indicates the error between Delft3D results and the value captured by Dyenamic. The red-shaded area indicates the error associated with time step varying between 0.3 and 0.7 s. (b) Validation of water density. Error associated with the water density computed by Dyenamic and the value obtained from Delft3D.

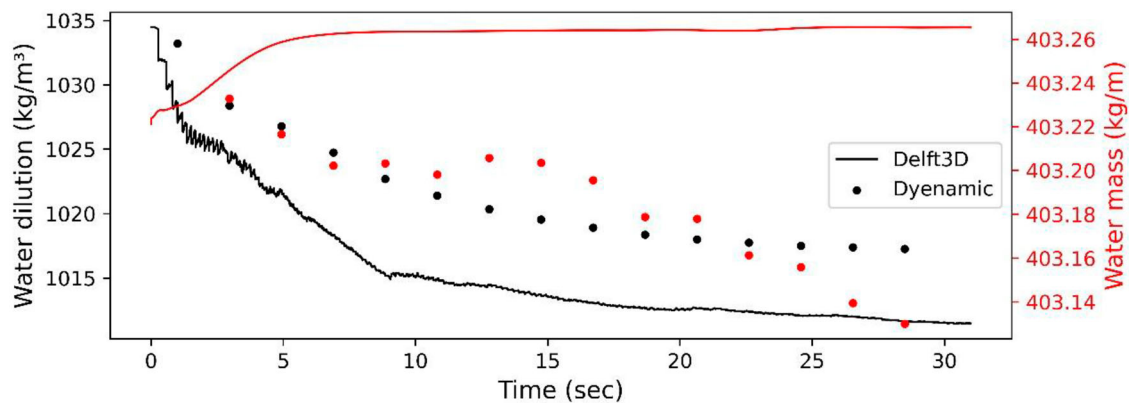


Figure 7. Dyenamic's capability evaluation. (a) Difference in current evolution between Delft3D and Dyenamic. The result from Delft3D has been interpolated onto Dyenamic's grid to allow error analysis. (b) Time-series of mass and water dilution for Delft3D and Dyenamic. Mass conservation was obtained through the integration of the density along the tank for each time step. The dilution was calculated by integrating the volume of gravity current volume ($\rho > 1015 \text{ kg m}^{-3}$).

is caused by the same mechanism as described above, in which the tracking neglects small concentration values for low-contrast images. Although this effect may lead to a loss of mass, the mass is sufficiently conserved by Dyenamic, indicating a mean error of 0.02%, equivalent to a mean density loss of 0.31 kg m^{-3} , compared to the mean water mass detected by the simulation.

Fluids from gravity currents are diluted mainly because of the recirculation that occurs in the current head (Hacker et al. 1996). As the current progresses, the ambient fluid is pushed by the current, creating a flow above the head. As pressure decreases, there is an entrainment mechanism of ambient water in the head, which contributes to interfacial instabilities and boundary exchange, increasing the dilution of the gravity current head (Balasubramanian and Zhong

2018). Although this mechanism occurs essentially during the self-similar phase (Hacker et al. 1996; Hallworth et al. 1996), Kelvin-Helmholtz billows generated immediately after lock release may also promote mixing between ambient and current fluids. Analysis of the displacement of the overturn density from Dyenamic indicates the generation of strong overturns of 10 cm right after lock release. This analysis corroborates the strongest dilution observed during the inertial slumping phase (Figures 5 and 7). The dilution was estimated by calculating the mean water mass of the gravity current, assuming that only the water density above $\rho = 1015 \text{ kg m}^{-3}$ was calculated as part of the gravity current. Dyenamic captured the same dilution mechanism observed in the Delft3D results, presenting a difference of less than 0.5% (Figure 7).

4.1.2. PIV measurement

To demonstrate results obtained with the PIV coupled with Dyanamic, a constant volume lock release of full-depth experiment was carried out with the same setup discussed in Section 4.1.1 and illustrated in Figures 2 and 3. However, before the gate was removed, seeding particles were added at the bottom of the channel. We used black pepper with a diameter of 2 mm and a density of approximately 1012 kg m^{-3} as seeding material for PIV measurements.

In this study case, laser sheets and high-resolution CMOS cameras were not used. A simple experimental setup was chosen to demonstrate that even for low-cost systems, the main feature of gravity current may be revealed. To record the propagation of the gravity current, a digital camera (Nikon D810 36.3 megapixels with a pixel size of $4.88 \mu\text{m}$) was placed 120 cm from the gate, covering a frontal area of $40 \times 20 \text{ cm}^2$.

The video from the analyzed area was processed with Dyanamic, which we enabled with the PIV measurement option. Based on tests performed earlier, we defined the best PIV calibration parameters. The detailed procedure to find the appropriate PIV calibration parameters is available in the user manual (de Carvalho Bueno et al. 2021). All calibration parameters, as well as the recorded video, additional output results, and the setting file, are available in the supplemental material of this article. Although Dyanamic provides PIV measurements in the resolution specified in the GUI, here we present only a detailed analysis for a pair of frames, in which one of them is illustrated in grayscale in Figure 8(a).

The PIV measurements obtained from Dyanamic can be decomposed into horizontal (Figure 8(b)) and vertical components (Figure 8(c)). From the horizontal velocity field, we may observe the typical horizontal motion of gravity currents, in which the heavier water moves in one direction, whilst the ambient water moves in the opposite direction (Figure 8(b)). This flow creates a shear layer that favors instabilities and boundary exchange and generates Kelvin-Helmholtz billows near the rear of the gravity current head. These billows are not clearly evidenced in the PIV measurements depicted in Figure 8(d) due to the resolution of the PIV measurements. Since the number of tracker particles is relatively small, the spatial resolution is limited by a relatively large interrogation window.

Although we were unable to observe the instabilities in hearing of the gravity current, we may detect the entrainment process, which is characterized by the downward velocities at the rear of the head (Figure 8(c)). The entrainment mechanism is

responsible for increasing the mixing between ambient and current fluids and favoring an increase in the current head volume.

Based on the Dyanamic tracker algorithm, the horizontal velocity obtained from PIV measurements at the current front can be compared with the front velocity detected by the tracker, also coupled with the software (Figure 9). The velocity estimated with the PIV method presents a higher fluctuation, which may be generated by the formation of billows. However, most of the time the front velocity is within the standard deviation of the PIV measurements.

4.1.3. Calibration of temporal resolution

Considering the camera specifications, a crucial aspect involved is performing a temporal calibration to determine the optimal time step required to obtain the best results with the software. This calibration is significant, because an excessively small Δt can hinder the camera's ability to discern the current evolution, resulting in multiple points with identical progress. By performing temporal calibration, we determine the ideal interval for Δt that ensures a smooth and accurate identification of the current evolution. To establish the most suitable temporal resolution for the software, we devised a formula,

$$\Delta t = \frac{\Delta x N}{u}, \quad (6)$$

where Δt is the time step defined by the user, Δx is the distance traveled by the current in each time step, u is the mean velocity of the current, and N is the minimum number of frames that must be used to obtain the best results from the software due to the frame rate of the camera (FPS).

To illustrate the impact of temporal resolution on the evolution of the gravity current, we applied the video of the simulated gravity current mentioned above ($\Delta x = 0.24 \text{ cm}$) with an average velocity of 6 cm s^{-1} using various temporal resolutions for data processing. We assessed three distinct temporal resolutions based on the recorded video and the characteristics of the gravity current. Using Equation 6 with $\Delta t = 0.1$ second, 0.5, and 2.0 s, we obtained 3, 13, and 50 frames, respectively, for each time step (Figure 10). It should be noted that with a small Δt , the front velocity can be poorly detected, resulting in inaccurate results due to limited spatial resolution. On the contrary, with a large Δt , the front velocity is well represented, but small fluctuations can go undetected due to the reduced temporal resolution.

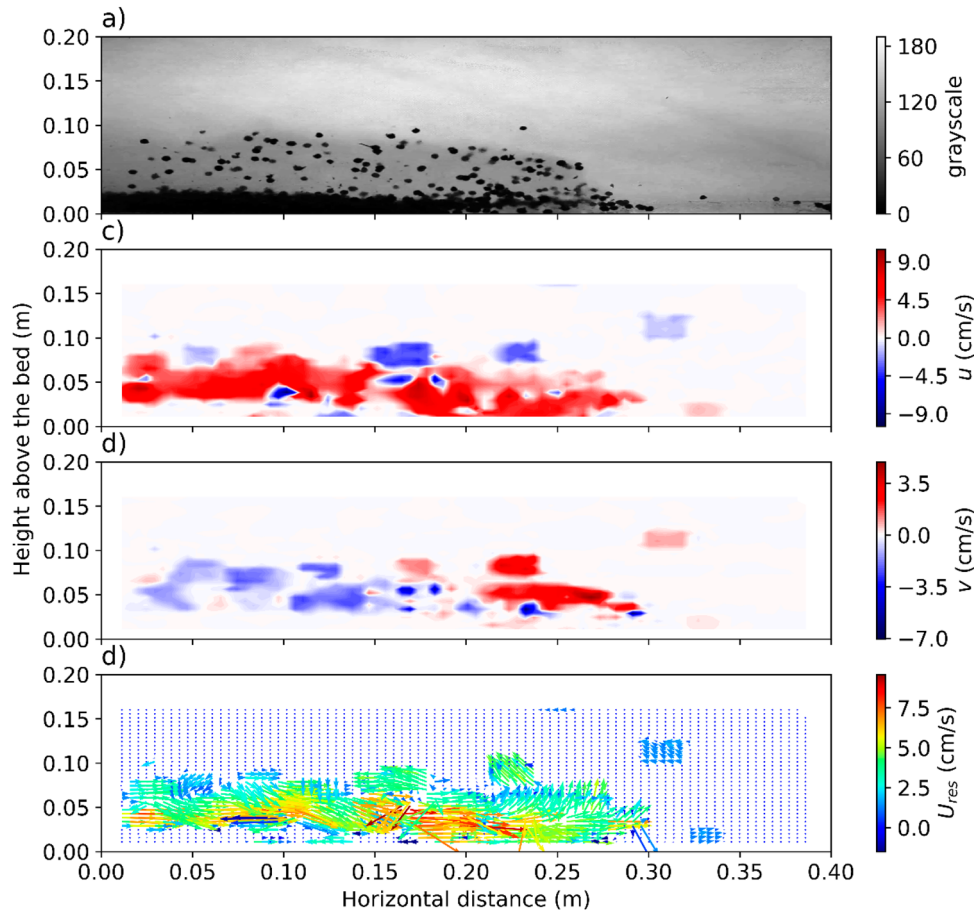


Figure 8. The velocity field estimated by Dyanamic from PIV measurements for frames 49 and 50. (a) Frame 49 in grayscale. Fields of (b) horizontal (u) and (c) vertical (v) velocities. (d) Velocity vector, in which the color indicates the magnitude of the resultant velocity (U_{res}). Vector velocities have been processed by removing outlier vectors identified by the software and neglecting velocities higher than 50% of the front velocity predicted by the tracker model.

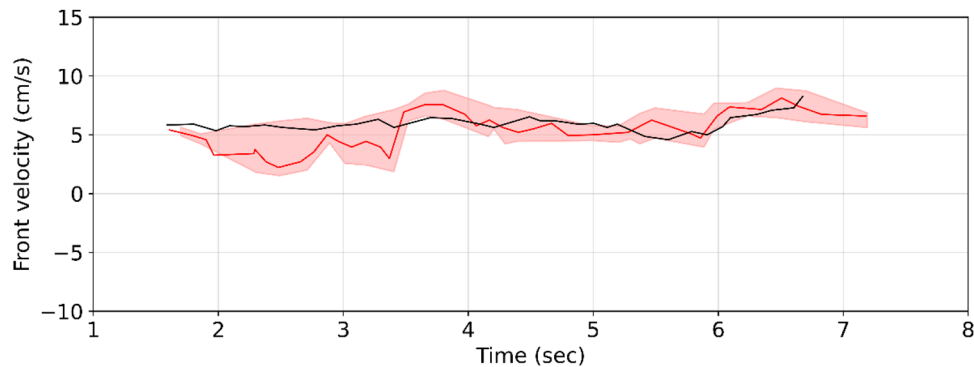


Figure 9. Temporal comparison between the front velocity of the current estimated by the tracker and PIV methods. The solid black line indicates the 1 s moving average front velocity estimated by the tracker algorithm. The solid red indicates the mean horizontal velocity estimated by the PIV for a small window (13.5 mm long and 18 mm high) defined at the current front, in which the red shaded area indicates the standard deviation of velocity measured within the PIV window.

The values presented above represent only the experiment. However, we conducted multiple tests with varying temporal resolutions. Our findings indicate that the optimal number of frames required to achieve the best

software results, considering the frame rate of the camera (FPS), is $N = 12$ (Figure 10). Therefore, we adopt $N = 12$ as a reference value. If the user selects a temporal resolution that results in $N \leq 12$, the program

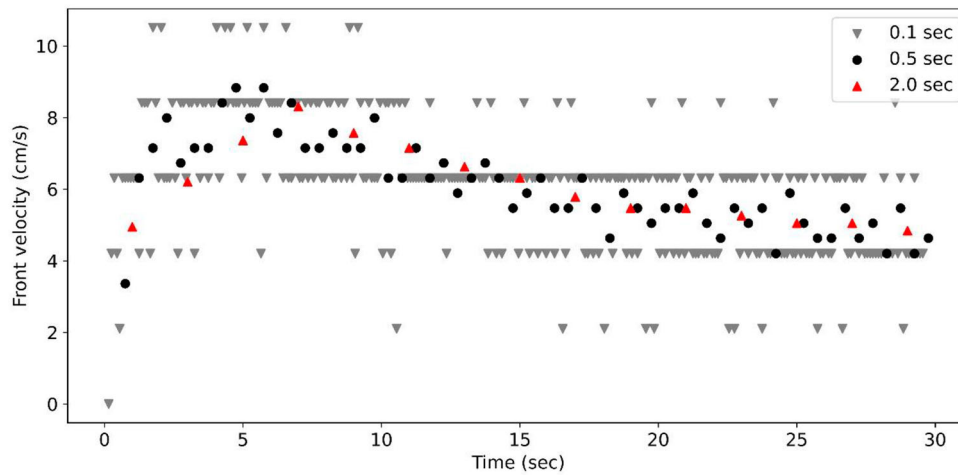


Figure 10. Graphical representation of the mean velocity variation using different time steps. We may notice that using small times like 0.1 s produce some steps. When we increase the time, the mean velocity becomes more reliable. However, if we increase the timestep too much, a part of the information may be lost because when the software detects a point, the current has already passed. We can see this behavior in $t = 2.0$ s.

provides a warning message, advising the user of the optimal value of Δt to effectively characterize the evolution of the gravity current (enforcing $N = 12$). It is important to note that the program can still be executed with a lower value of Δt . However, this may lead to potentially inaccurate results, due to the user's choice of a small temporal resolution, which could pose problems considering the camera's spatial resolution.

4.1.4. Calibration sensitivity

The accuracy of the results produced by the software is heavily dependent on the grayscale values utilized. Therefore, meticulous calibration becomes imperative prior to generating the results. In this context, a sensitivity analysis was conducted, beginning with a manual optimization of the experiment's calibration. This involved carefully observing the movement of the entire stream frame by frame within the tank. The process was replicated for three distinct experiments. Optimal calibration is deemed successful when there are no visible stains caused by grayscale variations throughout the entire passage of the current, while also preserving the integrity of the current.

Once the optimal values were determined, two different scenarios were created by changing the grayscale values. This involved both overestimating and underestimating the predominant values identified. The procedure was carried out separately for the grayscale of the stream and sediment, with each scenario involving grayscale changes of approximately 10% above and below the optimal values. It is important to note that during the current sensitivity analysis, the optimal values of the sediment were preserved, and, similarly,

during the sediment sensitivity analysis, the optimal values of the current were maintained.

Figure 11 visually illustrates the impact of grayscale changes on the frames, which influenced the results obtained by Dynamic. Changes in the upper limit of the grayscale impact only the front velocity and the evolution of the gravity current, leaving the sediment dynamics unaffected. Overestimated and underestimated calibrations resulted in a 10.11% increase and a 2.54% decrease in the average front velocity, respectively, presenting a mean root mean square error of 3.41 cm s^{-1} and 1.76 cm s^{-1} , respectively.

The alterations in the front velocity occur due to modifications in the shape of the gravity current (Figure 11). When the grayscale of the gravity current is overestimated, the current velocity tends to increase because of an expansion of the interface ahead of the current. This interface is highly sensitive to grayscale, slight values can cause the software to interpret environmental elements as part of the current. Similarly, when the background grayscale is underestimated during the gravity current calibration, this interface vanishes, leading to a decrease in speed but sacrificing the integrity of the current. These dynamics elucidate why the error obtained in the underestimation scenario is smaller than that in the overestimation scenario.

The sediment sensitivity analysis followed a procedure like that of the stream. After obtaining the optimal value, two additional scenarios were created by underestimating and overestimating the grayscale values of the sediment. In both scenarios, the grayscale variations were set at approximately 10% of the original value.

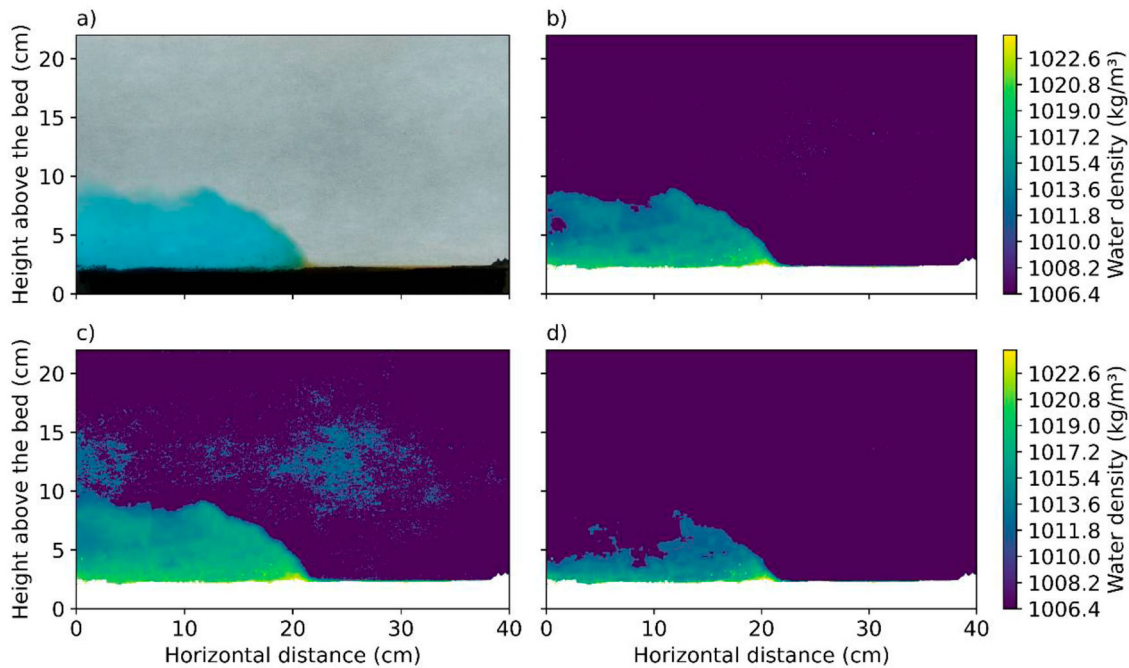


Figure 11. (a) An original frame taken from the video, (b) represents a result obtained from Dyanamic with a good calibration procedure, (c) represents a result with a grayscale 10% higher than that used in figure a, and (d) represents a result with a grayscale 10% lower than that used in figure a. It is possible to observe the existence of stains outside the current when the calibration is overestimated (c) and the loss of current integrity when the calibration is underestimated (d).

Shear stress, depending on the properties of the sediment and the condition of the gravity current, can promote intense ejection and burst events, leading to erosion and transport of the load from the bed (Zordan et al. 2019). To verify the resuspension of sediments, Dyanamic identifies specific longitudinal points and tracks the sediment variation relative to its initial state at each time step. It is important to note that, in certain instances, the initial values of sediment variation at the current's entrance may be negative, as the current tends to excavate the sediment. Throughout the current displacement, no significant variation in sediment was observed. The standard deviation of the total sediment resuspended from the overestimated calibration was 0.32 mm^2 (with a root mean square error of 0.48 mm^2), while for the underestimated calibration the standard deviation was 0.08 mm^2 (with a root mean square error of 0.26 mm^2), respectively.

To examine the mass variation within the system, the water mass values were calculated for each vertical column at every point (x, z). The sediment mass was integrated throughout the domain to determine the total water mass within the system. The objective was to observe any changes in mass when the system calibration varied and assess the degree of mass conservation deviation that occurs when the calibration values are underestimated or overestimated. The ideal scenario entails perfect mass conservation, and

analyzing these variations helps to evaluate the level of mass conservation achieved. Figure 12 shows the results of this comparison. It is possible to infer that the underestimated calibration tends to have a smaller difference in relation to the ideal calibration, which occurs for both analyses, current (Figure 12(a)) and sediment (Figure 12(b)).

4.2. Software availability and performance

Dyanamic is an open-source software developed in Python and released under the MIT General Public License. While the software can be run directly in a Python interpreter, it also provides a user-friendly graphical interface. To run Python scripts, Dyanamic requires a minimum version number of Python 3.7 and the following packages: tk (tkinter) 8.6.8, Numpy 1.16.3, Nitime 0.7, OpenCV 4.5.2, OpenPIV 0.23.6, and Matplotlib 3.1.0, or compatible versions. For a streamlined installation process, we recommend using the Anaconda package, as it includes many of the required packages by default. Further instructions on running Dyanamic can be found in the Supplementary Information for more detailed guidance.

Dyanamic was run for all case studies presented in sections 4.1.1 and 4.1.3 on an Intel(R) Core(TM) i7-1065G7 CPU 1.30 GHz processor with 32 GB installed physical memory. We use a version number

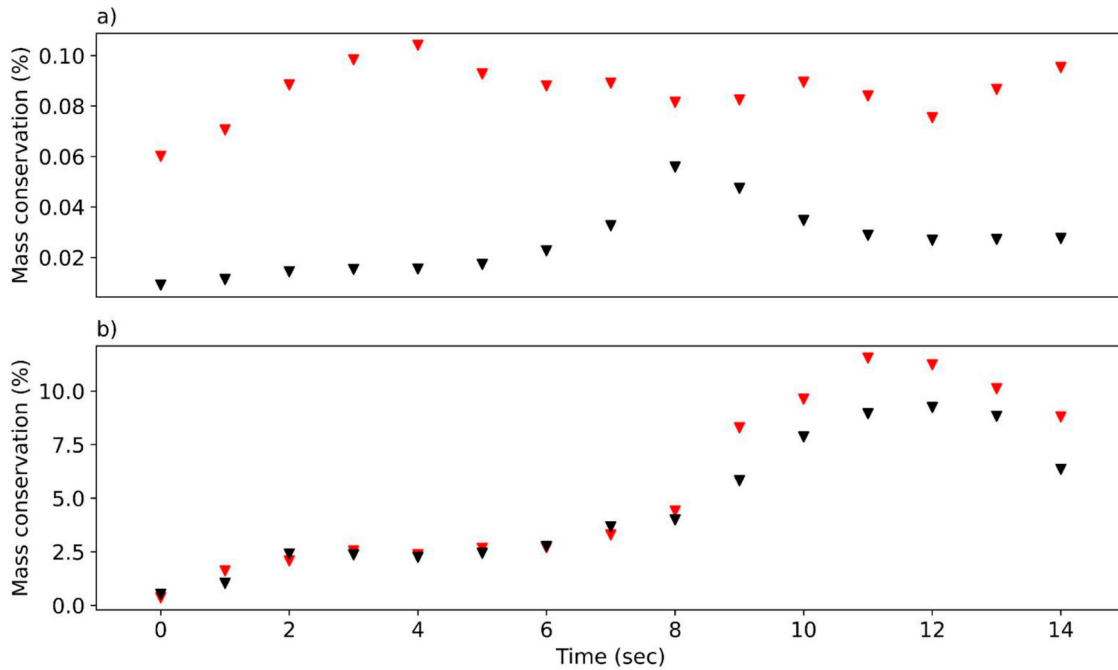


Figure 12. Difference between the current mass conservation with the calibration considered ideal for the overestimated (red) and underestimated (black) calibrations. Mass conservation related to (a) water density and (b) sediment particles.

of Python 3.7.6 bundled with Anaconda 3 (IPython 7.16.1). The details of how to set up laboratory experiments are provided in the user manual, and all data used in both experiments are available in the supplemental material.

When Dynamic starts the data processing, the software provides an interactive panel that displays an estimate of the time required for the analysis and the projected completion time. In the first case study discussed in Section 4.1.1, a video file lasting 60 s was analyzed, with a resolution of 985×88 pixels. Dynamic was configured to process the recorded video using a time step of 0.5 s and generate graphical output files with a resolution of 100 dots per inch (DPI). The program completed its execution in approximately 300 s and generated a total data size of 16 MB, including figures and text files. It is important to note that for this specific case study, PIV measurements were disabled.

4.3. Limitations and distinct applications

Modern studies on gravity currents in laboratory flumes often utilize sophisticated techniques such as Laser-induced Incandescence Fluorescence (Parsons and Garcia 1998; Martin and Garcia 2009) and PIV-Scalar (Gerber et al. 2011) to investigate the three-dimensional nature of these flows.

Due to turbulence, mixing at the current head and the inherently unsteady behavior of the flow, determining the height of the current and other properties can

be challenging in 2D images, leading to some uncertainties in computing the Froude number of the front Fr_ϕ (Marino et al. 2005), mixing processes, and many other variables. Although Dynamic is based on analyzing colored gravity currents and is susceptible to these uncertainties, the software offers a direct comparison with well-established theoretical results to assess the quality of the output data. In addition, simple 2D image analysis combined with colored gravity currents can still reveal important physical properties and reveal influences of gravity currents that are not yet well understood (Härtel et al. 2000).

Although the software has been designed primarily to investigate gravity currents in rectangular tanks, it can also be applied to various other color-dyed flows, including plumes, jets, and internal waves. In such cases, the software generates output files that are specific to gravity current experiments. However, for different applications, density maps and PIV measurements can be easily utilized. For specific examples of Dynamic's application to other color-dyed flows, please refer to Dynamic's user manual (de Carvalho Bueno et al. 2021)

5. Conclusions

This paper introduces Dynamic, an open source user-friendly software designed to investigate the mixing and transport of colored stratified flows, particularly focusing on the evolution of gravity currents. The software

offers in-depth analysis ranging from gravity currents generated in laboratory experiments to numerical simulations, with the aim of simulating geophysical and industrial applications. The analysis provided by Dye-dynamic may help reveal various physical aspects of the transport and mixing induced by this type of stratified flows, such as sea breezes, avalanches, volcanic surges, sandstorms, and sediment-laden underflow. Various liquid discharges into lakes, reservoirs, rivers, estuaries, seas, and oceans exhibit an intrinsic nature where the density difference between the discharged fluid and the surrounding fluid significantly contributes to mixing and transport.

The Dye-dynamic is capable of analyzing these mechanisms through a user-friendly interface, combining quantitative analysis of the visualized flow with the theoretical basis of gravity currents. It reveals density and velocity fields, providing both theoretical insights and empirical data. Moreover, Dye-dynamic offers the processing of measurements to derive parameters such as front speed, current height, Froude number, Richardson number, overturn density displacement, and theoretical results for different current stages (slumping, self-similar, and viscous phases). Additionally, it is equipped with a particle image velocimetry (PIV) algorithm, which when the flow is seeded, may reveal the velocity field of the flow.

One of the advantages of Dye-dynamic over other general tools for analyzing stratified flows is its user interface. Designed to be intuitive, the software facilitates the analysis of gravity currents from laboratory experiments and numerical simulations. It can be seamlessly integrated into undergraduate courses, including laboratory or project classes, to illustrate and quantify the effects of mixing processes associated with stratified flows. This includes illustrating various liquid discharges from municipal, agricultural, domestic, and industrial sources, as well as natural events such as sea breezes, avalanches, volcanic surges, and sandstorms.

The Dye-dynamic features a user-friendly interface that does not require programming knowledge, making it a valuable tool for educational and scientific purposes. It proves particularly useful for calibration procedures in numerical simulations and for engineering and scientific applications focused on the transport and mixing of gravity currents and their influence on sediment transport.

Acknowledgements

This study was financed in part by the Coordenação de Aperfeiçoamento de Pessoas de Nível Superior – Brasil (CAPES) – Finance Code 001. RCB, NSS e ADS thank CAPES for the scholarships. TBB acknowledges the productivity stipend

from the National Council for Scientific and Technological Development – CNPq, grant number 312211/2020-1, call no. 09/2020.

Disclosure statement

No potential conflict of interest was reported by the author(s).

Funding

This work was supported by Conselho Nacional de Desenvolvimento Científico e Tecnológico [grant number 312211/2020-1, call 09/2020]; Coordenação de Aperfeiçoamento de Pessoal de Nível Superior [grant number Finance Code 001].

ORCID

Rafael de Carvalho Bueno  <http://orcid.org/0000-0003-4205-2119>

References

- Arrillaga JA, de Arellano JV-G, Bosveld F, Baltink HK, Yagüe C, Sastre M, Román-Cascón C. 2018. Impacts of afternoon and evening sea-breeze fronts on local turbulence, and on CO₂ and radon-222 transport. *Q J R Meteorol Soc.* 144(713):990–1011. doi:10.1002/qj.3252.
- Auer, AH Jr, Sand W. 1966. Updraft measurements beneath the base of cumulus and cumulonimbus clouds. *J Appl Meteorol.* 5(4):461–466. doi:10.1175/1520-0450(1966)005%3C0461:UMBTBO%3E2.0.CO;2.
- Azpiroz-Zabala M, Cartigny MJB, Talling PJ, Parsons DR, Sumner EJ, Clare MA, Simmons SM, Cooper C, Pope EL. 2017. Newly recognized turbidity current structure can explain prolonged flushing of submarine canyons. *Sci Adv.* 3(10):e1700200. doi:10.1126/sciadv.1700200.
- Balasubramanian S, Zhong Q. 2018. Entrainment and mixing in lock-exchange gravity currents using simultaneous velocity-density measurements. *Phys Fluids.* 30(5):056601. doi:10.1063/1.5023033.
- Ben-Gida H, Gurka R, Liberzon A. 2020. OpenPIV-MATLAB—an open-source software for particle image velocimetry; test case: birds' aerodynamics. *SoftwareX.* 12:100585. doi:10.1016/j.softx.2020.100585.
- Benjamin TB. 1968. Gravity currents and related phenomena. *J Fluid Mech.* 31(2):209–248.
- Bernhardt J, Kirillin G. 2013. Seasonal pattern of rotation-affected internal seiches in a small temperate lake. *Limnol Oceanogr.* 58(4):1344–1360. doi:10.4319/lo.2013.58.4.1344.
- Best JL, Kirkbride AD, Peakall J. 2001. Mean flow and turbulence structure of sediment-laden gravity currents: new insights using ultrasonic Doppler velocity profiling. *Part Gravity Curr.* 157–172. doi:10.1002/9781444304275.ch12.
- Buckee C, Kneller B, Peakall J. 2001. Turbulence structure in steady, solute-driven gravity currents. *Part Gravity Curr.* 173–187. doi:10.1002/9781444304275.ch13.
- Cantero MI, Lee JR, Balachandrar S, Garcia MH. 2007. On the front velocity of gravity currents. *J Fluid Mech.* 586:1. doi:10.1017/S0022112007005769.

- de Carvalho Bueno R, da Silva N, dos Santos A, Bleninger T. 2021. *Dyenaic*: user manual. *Deltares*. 2014. Simulation of multi-dimensional hydrodynamic flows and transport phenomena, including sediments.
- Eames I, Hogg AJ, Gething S, Dalziel SB. 2001. Resuspension by saline and particle-driven gravity currents. *J Geophys Res Oceans*. 106(C7):14095–14111. doi:10.1029/2000JC900146.
- Gerber G, Diedericks G, Basson GR. 2011. Particle image velocimetry measurements and numerical modeling of a saline density current. *J Hydraulic Eng*. 137(3):333–342. doi:10.1061/(ASCE)HY.1943-7900.0000304.
- Gerritsen H, De Goede ED, Platzek FW, Genseberger M, van Kester J, Uittenbogaard RE. 2007. Validation document Delft3D-FLOW; a software system for 3D flow simulations. The Netherlands: Delft Hydraulics, Report X, 356, M3470.
- Grundy RE, Rottman JW. 1985. The approach to self-similarity of the solutions of the shallow-water equations representing gravity-current releases. *J Fluid Mech*. 156:39–53. doi:10.1017/S0022112085001975.
- Hacker J, Linden PF, Dalziel SB. 1996. Mixing in lock-release gravity currents. *Dyn Atmos Oceans*. 24(1–4):183–195. doi:10.1016/0377-0265(95)00443-2.
- Hadad T, Gurka R. 2013. Effects of particle size, concentration and surface coating on turbulent flow properties obtained using PIV/PTV. *Exp Therm Fluid Sci*. 45:203–212. doi:10.1016/j.expthermflusci.2012.11.006.
- Hallworth MA, Huppert HE, Phillips JC, Sparks RSJ. 1996. Entrainment into two-dimensional and axisymmetric turbulent gravity currents. *J Fluid Mech*. 308:289–311. doi:10.1017/S0022112096001486.
- Hallworth MA, Phillips JC, Huppert HE, Sparks RSJ. 1993. Entrainment in turbulent gravity currents. *Nature*. 362(6423):829–831. doi:10.1038/362829a0.
- Härtel C, Meiburg E, Necker F. 2000. Analysis and direct numerical simulation of the flow at a gravity-current head. Part 1. Flow topology and front speed for slip and no-slip boundaries. *J Fluid Mech*. 418:189–212. doi:10.1017/S0022112000001221.
- Huppert HE. 1982. The propagation of two-dimensional and axisymmetric viscous gravity currents over a rigid horizontal surface. *J Fluid Mech*. 121:43–58. doi:10.1017/S0022112082001797.
- Huppert HE. 2006. Gravity currents: a personal perspective. *J Fluid Mech*. 554:299. doi:10.1017/S002211200600930X.
- Huppert HE, Simpson JE. 1980. The slumping of gravity currents. *J Fluid Mech*. 99(4):785–799. doi:10.1017/S0022112080000894.
- Hutter K. 1996. Avalanche dynamics. In: *Hydrology of disasters*. Springer; p. 317–394. doi:10.1007/978-94-015-8680-1_11.
- Jkdrasik J, Kowalewski M. 2019. Mean annual and seasonal circulation patterns and long-term variability of currents in the Baltic Sea. *J Mar Sys*. 193:1–26. doi:10.1016/j.jmarsys.2018.12.011.
- Kyrousi F, Leonardi A, Roman F, Armenio V, Zanello F, Zordan J, Juez C, Falcomer L. 2018. Large Eddy Simulations of sediment entrainment induced by a lock-exchange gravity current. *Adv Water Res*. 114:102–118. doi:10.1016/j.advwatres.2018.02.002.
- Legg S, Briegleb B, Chang Y, Chassignet EP, Danabasoglu G, Ezer T, Gordon AL, Griffies S, Hallberg R, Jackson L., et al. 2009. Improving oceanic overflow representation in climate models: the gravity current entrainment climate process team. *Bull Am Meteorol Soc*. 90(5):657–670. doi:10.1175/2008BAMS2667.1.
- Liberzon A, Käufer T, Bauer A, Vennemann P, Zimmer E. 2020. *OpenPIV*. doi:10.5281/zenodo.4320056.
- Marino BM, Thomas LP, Linden PF. 2005. The front condition for gravity currents. *J Fluid Mech*. 536:49–78. doi:10.1017/S0022112005004933.
- Martin JE, Garcia MH. 2009. Combined PIV/PLIF measurements of a steady density current front. *Exp Fluids*. 46(2):265–276. doi:10.1007/s00348-008-0556-7.
- Mitxelena JAA. 2020. Impacts of sea-breeze fronts on local turbulence and scalar transport. In: *Thermally-driven mesoscale flows and their interaction with atmospheric boundary layer turbulence*. Springer; p. 71–99. doi:10.1007/978-3-030-48579-5_4.
- Ooi SK, Constantinescu G, Weber LJ. 2007. 2D large-eddy simulation of lock-exchange gravity current flows at high Grashof numbers. *J Hydraulic Eng*. 133(9):1037–1047. doi:10.1061/(ASCE)0733-9429(2007)133:9(1037).
- Paik J, Eghbalzadeh A, Sotiropoulos F. 2009. Three-dimensional unsteady RANS modeling of discontinuous gravity currents in rectangular domains. *J Hydraulic Eng*. 135(6):505–521. doi:10.1061/(ASCE)HY.1943-7900.0000034.
- Parker G, Garcia M, Fukushima Y, Yu W. 1987. Experiments on turbidity currents over an erodible bed. *J Hydraulic Res*. 25(1):123–147. doi:10.1080/00221688709499292.
- Parsons JD, Garcia MH. 1998. Similarity of gravity current fronts. *Phys Fluids*. 10(12):3209–3213. doi:10.1063/1.869848.
- Pickering KT, Underwood MB, Taira A. 1992. Open-ocean to trench turbidity-current flow in the Nankai trough: flow collapse and reflection. *Geology*. 20(12):1099–1102. doi:10.1130/0091-7613(1992)020%3C1099:OOTTTC%3E2.3.CO;2.
- Raffel M, Willert CE, Scarano F, Kähler CJ, Wereley ST, Kompenhans J. 2018. *Particle image velocimetry: a practical guide*. Springer. doi:10.1007/978-3-319-68852-7.
- Rottman JW, Simpson JE. 1983. Gravity currents produced by instantaneous releases of a heavy fluid in a rectangular channel. *J Fluid Mech*. 135:95–110. doi:10.1017/S0022112083002979.
- Scotti A, Pineda J. 2007. Plankton accumulation and transport in propagating nonlinear internal fronts. *J Mar Res*. 65(1):117–145. doi:10.1357/002224007780388702.
- Shin JO, Dalziel SB, Linden PF. 2004. Gravity currents produced by lock exchange. *J Fluid Mech*. 521:1–34. doi:10.1017/S002211200400165X.
- Simpson JE. 1982. Gravity currents in the laboratory, atmosphere, and ocean. *Ann Rev Fluid Mech*. 14(1):213–234. doi:10.1146/annurev.fl.14.010182.001241.
- Simpson JE, Britter RE. 1979. The dynamics of the head of a gravity current advancing over a horizontal surface. *J Fluid Mech*. 94(3):477–495. doi:10.1017/S0022112079001142.
- van der Wiel K, Gille ST, Llewellyn Smith SG, Linden PF, Cenedese C. 2017. Characteristics of colliding sea breeze

- gravity current fronts: a laboratory study. *Q J R Meteorol Soc.* 143(704):1434–1441. doi:[10.1002/qj.3015](https://doi.org/10.1002/qj.3015).
- Verso L, van Reeuwijk M, Gurka R, Diamessis PJ, Taylor ZJ, Liberzon A. 2017. Experimental study of the initial growth of a localized turbulent patch in a stably stratified fluid. *Int J Heat Fluid Flow.* 66:127–136. doi:[10.1016/j.ijheatfluidflow.2017.06.002](https://doi.org/10.1016/j.ijheatfluidflow.2017.06.002).
- Wynn RB, Masson DG, Stow DAV, Weaver PPE. 2000. Turbidity current sediment waves on the submarine slopes of the western Canary Islands. *Mar Geol.* 163(1–4):185–198. doi:[10.1016/S0025-3227\(99\)00101-2](https://doi.org/10.1016/S0025-3227(99)00101-2).
- Yarom E, Sharon E. 2014. Experimental observation of steady inertial wave turbulence in deep rotating flows. *Nat Phys.* 10(7):510–514. doi:[10.1038/nphys2984](https://doi.org/10.1038/nphys2984).
- Zordan J, Schleiss A, Franca MJ. 2019. Potential erosion capacity of gravity currents created by changing initial conditions. *Earth Surf Dyn.* 7(1):377–391. doi:[10.5194/esurf-7-377-2019](https://doi.org/10.5194/esurf-7-377-2019).